DOI: 10.1002/fuce.201900039

Effects of Clamping Pressure on Cold Start Behavior of Polymer Electrolyte Fuel Cells

A. M. Dafalla[1,2], L. Wei[1], Z. H. Liao[1,2], F. M. Jiang[1,3]*

[1] Laboratory of Advanced Energy Systems, CAS Key Laboratory of Renewable Energy, Guangdong Key Laboratory of New and Renewable Energy Research and Development, Guangzhou Institute of Energy Conversion, Chinese Academy of Sciences (CAS), 2 Nengyuan Rd, Wushan, Tianhe District, Guangzhou 510640, China
[2] University of Chinese Academy of Sciences, 19A Yuquan Rd, Shijingshan District, Beijing 100049, China
[3] Present address: Laboratory of Advanced Energy Systems, Guangzhou Institute of Energy Conversion, Chinese Academy of Sciences (CAS), 2 Nengyuan Rd, Wushan, Tianhe District, Guangzhou 510640, China

Received March 25, 2019; accepted May 13, 2019; published online June 12, 2019

Abstract

Understanding the cold start process of polymer electrolyte fuel cell (PEFC) is crucial to the development of an advanced PEFC of good cold start performance or to the design of advanced cold start strategies. In this study, a three-dimensional cold start model has been adapted and further developed to numerically investigate the cold start behavior under the applied clamping pressure, which was not considered in previous cold start modeling and simulation work. The PEFC cold start performance is studied under various assembly pressures in terms of polarization curves, ice formation, water content profile, and current density distribution, etc. The results indicate that, using a large clamping pressure leads to a significant decline on the cold start performance; therefore, using an optimum clamping pressure is important to obtain a better cold start performance. It is found that increasing the clamping pressure not only increases the ice accumulation in cathode catalyst layer, but also causes the dehydration of membrane and decreases the cold start performance. The proposed model can be used as a powerful tool to study the realistic cold start performance of PEFC and to assist the development of more advanced PEFC cold start strategies.

Keywords: Clamping Pressure, Cold Start, Computational Fluid Dynamic Analysis, Deformation, Fuel Cells

1 Introduction

Polymer electrolyte fuel cell (PEFC) is one of the most promising, cleanest, and highly efficient power sources, particularly for vehicles' applications due to their zero emissions. Despite the great efforts which have been made toward the commercialization of PEFC, there are still some major challenges remain to be overcome [1, 2]. An effective start-up from subfreezing environment is one of these barriers [3]. When a PEFC operates at a subzero temperature, if the produced water from the oxygen reduction reaction (ORR) cannot be timely removed, the accumulated water in the catalyst layer and gas diffusion layer turns to ice. The formed ice will limit the reactants transport in the catalyst layer/gas diffusion layer and reduce the electrochemical active area (ECA), which leads to the drop of cell voltage, or even shut-down of the cell if the ice formation reaches a threshold value [4]. Thus, better cold start performance of a PEFC becomes a significant factor for its commercialization [3].

Several parameters influence the successful startup of PEFC from subfreezing environment. Therefore, the ice formation phenomena under different cold startup temperatures were numerically and experimentally explored [5–16]. Moreover, self-startup strategies of PEFCs from various subfreezing conditions were suggested [17, 18]. Although the great efforts that have been done during the last decade, the cold start performance of PEFCs remains to be further improved before their wide commercialization.

To ensure the stability of fuel cell system, the different layers of PEFC are clamped together. The applied clamping pressure results in dimensional and physical changes in fuel cell components, although it is essential to decrease the contact resistance between the different layers and to prevent the leakage of reactants. This clamping pressure mainly affects the mechanical and physical properties of both anode and cathode gas diffusion layers due to their smaller Young's module compared to catalyst layers (CLs) and membrane [19]. Basically, the clamping pressure influences the thickness, porosity, permeability, and diffusivity of gas diffusion layer (GDL) [20]. Small clamping pressure generally causes a high contact electrical resistance between the bipolar

[*] *Corresponding author, fm_jiang2000@yahoo.com*

ORIGINAL RESEARCH PAPER

plate (BP) and GDL [21–24]. On the other hand, using a large clamping pressure may result in a plastic deformation on the entire cell [25]. Taymaz et al. [26] proposed that pressure values in a range of 0.5 to 1.0 MPa are the optimum ones when considering the electrical properties of fuel cell components. Chang et al. [27] experimentally examined the porosity, permeability, and thickness of GDL under various clamping pressures. They also measured the contact resistance between GDL and bipolar plate for the compressed cells. They found that increasing the clamping pressure leads to mass-transfer limitation between the flow channel (FC) and catalyst layer. Chi et al. [28] studied the influence of non-uniform GDL properties on the performance of PEFC under clamping pressure using both experimental and numerical approaches. Their results demonstrated that higher compression ratios lead to more vapor saturation, water flooding, and hydrogen deficiency downstream. Most recently, Yang et al. [29] investigated the effect of membrane electrode assembly design on ice/water distributions and output performance of cold startup operation by changing the contact angle of micro-porous layer (MPL), they considered different surrounding heat transfer coefficients, design parameters and structural properties in their analysis. They found that weakening the hydrophobicity of GDL enhances the water removal in MPL, hence preventing the MPL from water flooding.

Even though a number of cold start studies have been presented in literature, the clamping pressure effects on PEFC cold start behavior have not yet been studied to date. Therefore, the objective of this paper is to numerically investigate the cold start performance under different applied clamping pressures, particularly the focus is on studying the transport phenomena through the deformed GDL such as ice formation, water content profiles, heat generation, and current density distributions. We employed a simplified mathematical approach to predict the deformation, porosity, permeability and tortuosity changes of GDLs under various clamping pressures. Then a three dimensional computational fluid dynamics (CFD) model that was established for cold start simulation in a previous study [9] is adapted and further developed to predict the cold start behavior of PEFC under different clamped cases. Furthermore, the contact resistance between land and GDL is considered as a function of clamping pressure. The simulation results of various clamping forces are finally compared with the uncompressed case results to comprehend the effects of clamping pressure.

2 Numerical Model

2.1 PEFC Cold-start Model

In this study, a previously developed PEFC cold-start model by Jiang et al. [9] is further developed to explore the influence of clamping pressure on the PEFC cold start performance. A half single-channel geometry consisting of all subcomponents of PEFC: membrane, gas flow channels, current collectors, GDLs, and CLs is considered. The governing equations of PEFC cold-start model are summarized in Table 1. Source terms in each region are presented in Table 2. More details about the electrochemical, physical and transport properties can be found in [9, 15] and thus are not repeated here. The geometrical parameters, operating conditions, and material properties are described in Tables 3 and 4.

Table 1 PEFC cold start model: conservation equations.

Conservation Equations		
Mass	$\frac{\partial(\varepsilon_s\rho_s)}{\partial t}+\frac{\partial(\varepsilon\rho)}{\partial t}+\nabla\cdot(\rho\vec{u})=0$	(1)
Momentum	$\left[\frac{\partial(\rho\vec{u}/\varepsilon)}{\partial t}+\nabla\cdot\left(\frac{\rho\vec{u}\vec{u}}{\varepsilon^2}\right)\right]=\nabla\cdot(\mu\nabla\vec{u})-\nabla p+S_u$	(2)
Species	$\frac{\partial(\varepsilon C^i)}{\partial t}+\nabla\cdot(\vec{u}C^i)=\nabla\cdot\left(D^i_{eff}\nabla C^i\right)+S^i_c$	(3)
Charge	$\nabla\cdot\left(\kappa^{eff}_e\nabla_e\right)+S_e=0$	(4)
	$\nabla\cdot\left(\sigma^{eff}_s\nabla_s\right)+S_s=0$	(5)
Energy	$\left[\frac{\partial\left[\left(\rho c_p\right)_{cell}T\right]}{\partial t}+\nabla\cdot\left[\rho c_p\vec{u}T\right]\right]=\nabla\cdot\left(k_{eff}\nabla T\right)+S_T$	(6)

A generalized water transport equation is considered and solved for all regions of a fuel cell as follows:

$$\frac{\partial\left(\varepsilon_{eff}C^{H_2O}\right)}{\partial t}+\nabla\cdot\left(\bar{u}C^{H_2O}\right)=\nabla\cdot\left(D^{H_2O}_{eff}\nabla C^{H_2O}\right)+S^{H_2O}_C \tag{7}$$

ε_{eff} and $D^{H_2O}_{eff}$ can be written with respect to the physics taking place in different layers of the cell as:

$$\varepsilon_{eff}=\begin{cases}1.0 & \textit{Gas channels}\\ \varepsilon_0(1-s) & \textit{GDLs}\\ \frac{1}{EW}\frac{RT}{p_{sat}}\left(\rho+\lambda\frac{d\rho}{d\lambda}\right)\frac{d\lambda}{da} & \textit{Membrane}\\ \varepsilon_0(1-s)+\varepsilon_{mem}\frac{1}{EW}\frac{RT}{p_{sat}}\left(\rho+\lambda\frac{d\rho}{d\lambda}\right)\frac{d\lambda}{da} & \textit{CLs}\end{cases} \tag{8}$$

Table 2 PEFC cold-start model: source terms.

	Gas channels	Gas diffusion layers	Catalyst layers	Membrane
S_u	0	$-\frac{\mu}{K_{GDL}}\vec{u}$	$-\frac{\mu}{K_{CL}}\vec{u}$	–
$S_C^{H_2O}$	0	$-\dot{q}_{gs}^{H_2O}$	$-\nabla\cdot\left(\frac{n_d}{F}i_e\right)-\frac{s_k j}{nF}-\dot{q}_{gs}^{H_2O}$	$-\nabla\cdot\left(\frac{n_d}{F}i_e\right)$
S_c (for reactants)	0	0	$-\frac{s_k j}{nF}$	0
S_e	–	–	j	0
S_s	0	0	$-j$	–
S_T	–	$\frac{i_s^2}{\sigma_s^{eff}}+\dot{q}_{gs}^{H_2O}h_{gs}$	$j\left(\eta-T\frac{\partial(U_o)}{\partial T}\right)+\frac{i_e^2}{\kappa_e^{eff}}+\frac{i_s^2}{\sigma_s^{eff}}+\dot{q}_{gs}^{H_2O}h_{gs}$	$\frac{i_e^2}{\kappa_e^{eff}}$

Table 3 Cell dimensions and operation conditions.

Description	Value	Unit
Cell height; length	2; 600	mm
Land shoulder width	1.0	mm
Anode/cathode GDL thickness	300; 300	µm
Anode/cathode CL thickness	10; 10	µm
Membrane thickness	30	µm
channel depth; width	1; 1	mm
Initial water content	6.2	–
Startup temperature	253.15	K
Current density	1,000; 3,000	A m^{-2}
Anode/cathode stoichiometry	2.0	–
Anode/cathode inlet gas temperature	253.15	K
Anode/cathode pressure	1.0	atm

$$D_{eff}^{H_2O}=\begin{cases}D_g^{H_2O} & \text{Gas channels}\\ [\varepsilon_0(1-s)]^{1.5}D_g^{H_2O} & \text{GDLs}\\ D_{mem}^{H_2O}\dfrac{1}{EW}\dfrac{RT}{p_{sat}}\left(\rho+\lambda\dfrac{d\rho}{d\lambda}\right)\dfrac{d\lambda}{da} & \text{Membrane}\\ [\varepsilon_0(1-s)]^{1.5}D_g^{H_2O}+\varepsilon_{mem}^{1.5}D_{mem}^{H_2O}\dfrac{1}{EW}\dfrac{RT}{p_{sat}}\left(\rho+\lambda\dfrac{d\rho}{d\lambda}\right)\dfrac{d\lambda}{da} & \text{CLs}\end{cases}\quad(9)$$

$D_{mem}^{H_2O}$ and $D_g^{H_2O}$ represent the water diffusivity in the membrane phase and the gas phase respectively, defined as:

$$D_g^{H_2O}=D_0\left(\frac{T}{353.15}\right)^{\frac{3}{2}}\left(\frac{P_o}{P}\right)\quad(10)$$

$$D_{mem}^{H_2O}=\begin{cases}5.93\times10^{-5}\lambda\left(e^{0.28\lambda}-1\right)e^{\left(-\frac{4269}{T}\right)} & \text{if } 0<\lambda\leq3\\ 7.97\times10^{-6}\lambda\left(1+161e^{-\lambda}\right)e^{\left(-\frac{4269}{T}\right)} & \text{else}\end{cases}\quad(11)$$

2.2 Clamped GDL Properties Calculations

A simplified mathematical approach is considered to predict the porosity change in the deformed GDLs under different applied clamping pressures. Then, the influenced structural and transport properties of the compressed GDLs such as permeability and tortuosity are calculated based on the reduced porosity, and selectively applied for various cases in the cold start simulations to be presented later on.

The clamping pressure is applied on the top and bottom surfaces of bipolar plates and assumed to be uniformly distributed. Due to the higher Young's module of both membrane and catalyst layer compared to the GDL, their deformation by assembly pressure can be neglected [23, 26]. Therefore, we assume that the applied clamping force results only in the deformation of pore volume of gas diffusion layers while the solid volume remains constant, as shown in Figure 1, reducing the pore volume directly decreasing the GDLs porosity. In addition, the GDL intrusion into the channels is neglected in this investigation [30] and will be considered in future work.

We can determine the porosity variation of GDL after applying the clamping pressure as:

$$\varepsilon_{com}=\varepsilon_o\frac{V^{com}-V^{solid}}{V^i-V^{solid}}\quad(12)$$

with

$$V^i=width*length*height(L)\quad(13)$$

$$V^{solid}=V^i(1-\varepsilon_o)\quad(14)$$

$$V^{com}=width*length*height(l_{com})\quad(15)$$

where V^{com} is the volume of the compressed GDL, V^{solid} is the volume of solid material, V^i is the initial volume of the GDL before applying the clamping pressure, ε_0 and ε_{com} are the porosities of the GDL before and after the GDL compression, respectively.

ORIGINAL RESEARCH PAPER

Table 4 Material and transport properties.

Description	Value	Unit
Porosity of GDL (initial); CL	0.6;0.53	–
Volume fraction of ionomer in CL	0.15	–
Density of gas mixture	1.0	kg m^{-3}
Heat capacity of Membrane; CL; GDL; bipolar plate	1,650; 3,300; 568; 1,580	kJ m^{-3} K^{-1}
Heat conductivity of Membrane; CL; GDL; bipolar plate	0.95; 1.0; 1.0; 20	W m^{-1} K^{-1}
Heat capacity of ice; frost	3,369.6	kJ m^{-3} K^{-1}
Heat conductivity of ice; frost	2.4	W m^{-1} K^{-1}
Latent heat of desublimation	5.1 × 10^{4}	J mol^{-1}
Permeability of CL	1.0 ×10^{-13}	m^{2}
Electronic conductivity of GDL; CL; bipolar plate	300; 300; 1×10^{7}	S m^{-1}
Equivalent weight of ionomer	1.1	kg mol^{-1}
Density of dry membrane	1,980	kg m^{-3}
H_2/H_2O diffusivity in anode	8.67×10^{-5}; 8.67×10^{-5}	m^{2} s^{-1}
O_2/H_2O diffusivity in cathode	1.53×10^{-5}; 1.79×10^{-5}	m^{2} s^{-1}
GDL Young's modulus (E)	6.2 [22]	MPa

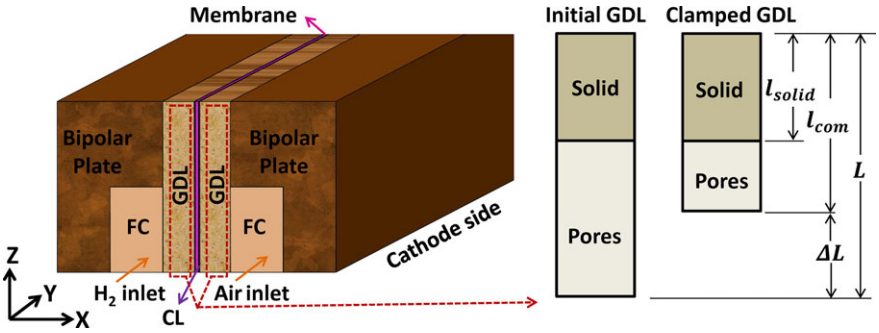

Fig. 1 Computational domain for a half single cell before applying clamping force and the assumed model for clamped GDL.

ΔL is the deformation of GDL due to compression, and can be calculated using a simplified form of Hooke's law as:

$$\Delta L = \frac{P_{contact}\, L}{A_{contact}\, E} \tag{16}$$

where E is the Young's modulus, $P_{contact}$ is the contact pressure that can be determined by:

$$P_{assembly}{}^{*}A_{assembly} = P_{contact}{}^{*}A_{contact} \tag{17}$$

where the $P_{assembly}$ and $A_{assembly}$ are the assembly pressure and the area on which this assembly pressure is applied, respectively. $A_{contact}$ is the contact area on which the contact pressure is applied.

Based on the modified porosity of clamped GDL, the permeability of the compressed GDL can be obtained by using the well-known Kozeny-Carman relation [31] as:

$$K = \frac{\left(D_f\right)^2 (\varepsilon_{com})^3}{16\, K_{ck} (1-\varepsilon_{com})^2} \tag{18}$$

where D_f is the diameter of fibers forming the GDL, K_{ck} is the Kozeny-Carman constant. Another structural parameter related to the porosity change is the tortuosity of GDL material, which is considered as [32]:

$$\tau = 1 - 0.49 \ln(\varepsilon_{com}) \tag{19}$$

The contact resistance ($R_{contact}$) can be calculated as [23]:

$$R_{contact} = 2.2163 + \frac{3.5306}{p_{contact}}\ \text{m}\Omega\ \text{cm}^2 \tag{20}$$

Then the contact resistance between GDL and current collector is included for various compressed cases through modifying the electronic conductivity in the computational cells of the current collector interfacing with GDL. The modified electronic conductivity of current collector at a nodal point facing GDL is given by:

$$\sigma' = \frac{1}{(1/\sigma + R_{contact}/\Delta x)} \tag{21}$$

where σ is the electronic conductivity of the current collector (original value), and Δx is the cell size.

2.3 Numerical Procedure

First, we predict the GDL deformation and GDL porosity change under various applied pressures. Then, we calculated the permeability and tortuosity of GDL as a function of the reduced porosity for various cases. Table 5 describes the modified GDL's properties due to clamping pressures. After that, we employed a three dimensional (3D) cold start model by using ANSYS-Fluent based on CFD method. The conservation equations and different source terms are implemented through customizing its user defined functions (UDFs). The geometry, mesh and time step sizes for cold start simulation are based on the work by Mao et al. [15, 33], in which the numerical accuracy has been extensively evaluated.

Table 5 GDL's properties variation under clamping pressures.

Cases	Clamping pressure / MPa	Compression ratio / %	Porosity / ε_{com}	Permeability / m^2	Tortuosity
Case 1	–	–	0.6	1.05× 10^{-12}	1.25
Case 2	0.5	16	0.44	1.39× 10^{-13}	1.4
Case 3	1.0	31	0.28	2.16× 10^{-14}	1.62
Case 4	1.5	47	0.12	1.14× 10^{-15}	2.04

2.4 Boundary and Initial Conditions

Dry air and hydrogen are fed into the cathode and anode channels. The reactant species in gas channels and GDLs are initially set to have the same molar concentration as the inlet gas. The bipolar plate temperature (at anode and cathode side) is kept constant at the startup temperature (T = 253.15 K). Zero flux boundary condition is applied to the electrolyte phase potential, while for the electronic phase potential, a reference potential (zero) is set at the anode side, and a constant current density of 1,000 or 3,000 A m^{-2} is prescribed at the outer surface of the cathode bipolar plate to start up the cell. At the channel inlets, the gas velocity u_{in} can be calculated from the stoichiometric flow ratio, i.e., ξ_a or ξ_c, defined at the current density, I, namely:

$$\xi_a = \frac{C^{H_2} u_{in,a} A_{in,a}}{IA/2F}, \quad \xi_c = \frac{C^{O_2} u_{in,c} A_{in,c}}{IA/4F} \tag{22}$$

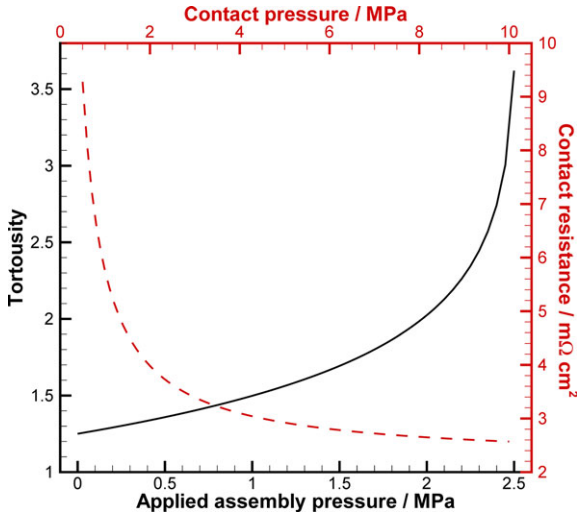

Fig. 2 Correlation between the clamping pressure and tortuosity, and the contact pressure and contact resistance for fuel cells.

3 Results and Discussion

3.1 Effects of Clamping on GDL Properties and Contact Resistance

Eight cases are calculated considering uncompressed cell and cell assembly pressures of 0.5 MPa, 1.0 MPa, and 1.5 MPa, respectively, under both low and high current densities. The uncompressed case presents the non-deformed GDLs in which the original GDL thickness and porous properties such as porosity and permeability remain the same, and it is the most commonly used case in previous studies of cold start modeling and simulation [9, 34, 35]. The GDL deformation and porosity changes after applying clamping pressures can be seen in Table 5. 16% of the initial GDL thickness is deformed under the 0.5 MPa pressure application, and when the clamping pressure is increased to 1.5 MPa the GDL deforms to the half (47%). As we present in Section 2.3, we calculate the clamped GDL porosity as function of clamping pressure. Then we obtain the permeability and tortuosity of the clamped GDL based on the new calculated porosity. Different GDL porosity profiles are considered in this study. For cases 2, 3, and 4 the porosity values of GDL change only under the land owing to applied pressure under the land, while the porosity under the channel remains as its intrinsic value (0.6).

The relation between contact pressure and contact resistance is also shown in Figure 2, the presented curve illustrates the significance of applying a proper contact pressure to compact the fuel cell layers in order to reduce the contact resistance between them. It is observed that increasing the applied pressure results in decrease of the contact resistance, which is mainly due to the increased contact area in the interface between GDL and land. Moreover, the drop rate of contact resistance is severe within the range of 0.5 to 2.0 MPa, and after that the curve shows a slight drop, mainly because there is no large increase in the contact area after that range of contact pressures. On the other hand, Figure 2 indicates that increasing the assembly pressure increases the GDL tortuosity due to the reduced porosity and thickness of GDL.

3.2 Effects of GDL Compression on Cold Start Behavior

In this study, we consider a non-isothermal model with constant boundary temperature. The fixed constant temperature boundary condition denotes that bipolar plates' temperatures on both anode and cathode sides are kept constant at the startup temperature (–20 °C) but the temperature of the catalyst layer is slightly higher due to the generated heat from the chemical reactions. This boundary condition simulates the end cell of the fuel cell stack where the external wall of the bipolar plate remains at the start up temperature. By using this quasi-isothermal operating condition, the cold start operation is destined to shut down. However, it is useful to evaluate the cold start capability of PEFCs [4, 15, 36]. Under this scenario, the produced water from ORR and fundamental data of cold start cell can be quantified before the cell shutdown. Thus, the measured data becomes independent of the cell fixture and its thermal mass, and depends more in the intrinsic properties of the cell. More details and discussion about the constant temperature boundary condition can be found in Tajiri et al. [10, 37].

In the catalyst layer, where the water produces, under subzero temperatures the ice accumulation further obstructs the oxygen to the catalyst layer. Even though, when the ice formation is still low, the cell voltage increases due to the small rise in the temperature from the chemical reaction and also due to the hydrated membrane, until the ice formation reaches a certain threshold level (ice fraction in pore volume is about 1), leading the cell to shut down. Consequently, the unsuccessful startup from –20 °C because the temperature cannot reach the freezing point before the cathode CL is filled up by ice [38].

Figure 3 depicts the oxygen concentration distribution in the y–z plane at the middle of the cathode GDL along the flow

direction for different cases. For all cases along the flow path, from inlet to outlet the oxygen concentration continuously decreases because of the oxygen consumption in cathode CL. We observe that the uncompressed case shows more even distribution of oxygen due to the constant GDL properties under land and channel. Besides, we note that when we apply a higher clamping pressure it becomes more difficult for oxygen to transport from gas channel to CL *via* GDL, especially in the region under land, and that is mainly because of the reduced porosity and permeability of GDL under the land.

Figures 4 and 5 depict the ice fraction contours at the center of the cathode CL for various cases at different time instants in *y*–*z* plane along the flow direction and *x*–*z* plane at the middle of the cell length, respectively. In the uncompressed cases: case 2 and case 3, the ice tends to accumulate more under the land area than under the channel area due to the higher current density in the region under land compared to the region under channel. A comparison of cases 1, 2, and 3 where the thicknesses of GDLs are reduced by 0%, 16%, and 31%, respectively, further elucidates the influence of clamping pressure on ice formation behavior in cold start process. It is found that applying a higher clamping pressure results in slightly larger amount of ice in the cathode catalyst layer, mainly because the accumulated water under the land is more difficult to be expelled due to the reduced porosities, that leads to longer water transport path in cases 2 and 3 compared to the uncompressed case.

In Case 4 where the GDL compression ratio is equal to 47%, the ice fraction accumulates faster near the channel region (see Figures 4 and 5). This trend can be illustrated as follows, the severe oxygen transport limitation under the land due to the reduced GDL porosity in case 4 (see Figure 3), greatly lowers the current density under the land (see Figure 7), which in turn results in relatively higher current density profile under the channel region along the flow direction owing to the imposed constant operating current load. Consequently, the higher current density profile under the channel region results in more water production, as well as more ice formation rate under the channel than that under the land. In addition, the existence of higher current density profile under the channel causes the water flow from the anode side to the cathode side *via* electro-osmotic drag (EOD) effect. The EOD effect due to the clamping pressure can be clearly observed from water content profiles for both clamped and uncompressed cases in Figure 6, in the clamped case owing to the higher current density under the FC, the EOD makes the membrane water content decrease in the region

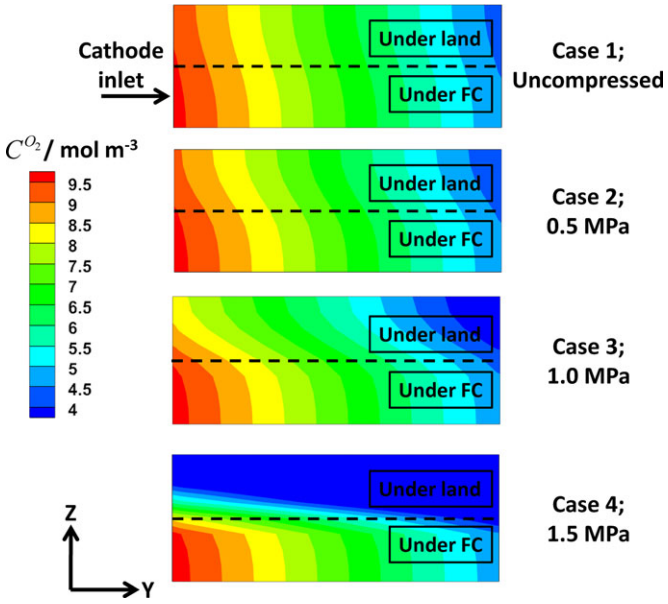

Fig. 3 Oxygen concentration contours in the *y*–*z* plane at the middle of the cathode GDL for cases 1–4 at t = 30 s under an operating current density of 1,000 A m^{-2}.

neighboring to the anode CL side, thus in turn leads to the dehydration of the membrane.

The membrane current density contours under different operating load current for various cases are plotted in Figure 7. The current density distribution in the cell depends on both charge and mass transport. The current density distributions for all cases decline along the flow direction due to oxygen depletion. Moreover, the transfer current density is higher under the land region for case 1 and case 2. This distribution is dominated by the transport of protons and electrons. In the

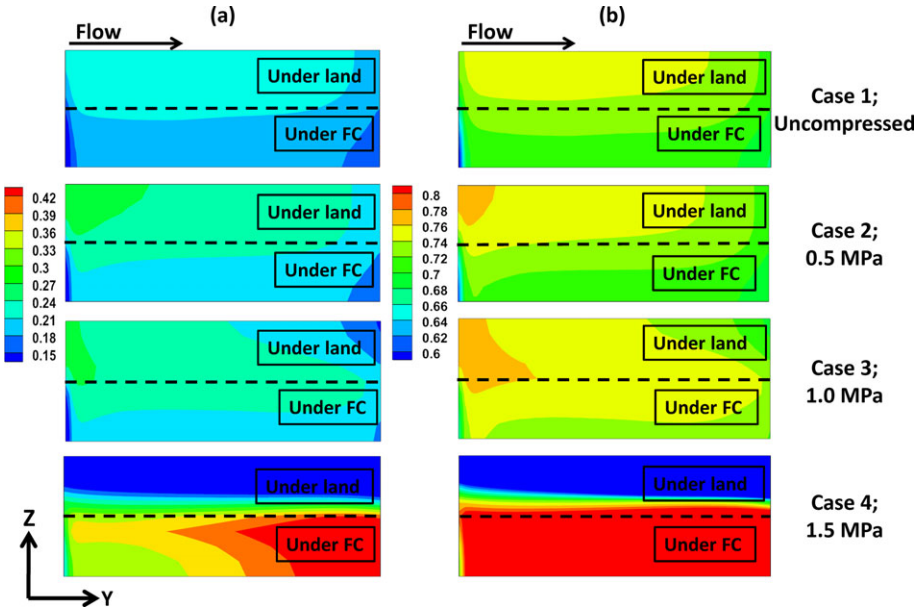

Fig. 4 Ice fraction contours in the *y*–*z* plane at the center of the cathode CL for cases 1–4 at different time (a) t = 50 s, (b) t =76 s under an operating current density of 1,000 A m^{-2}.

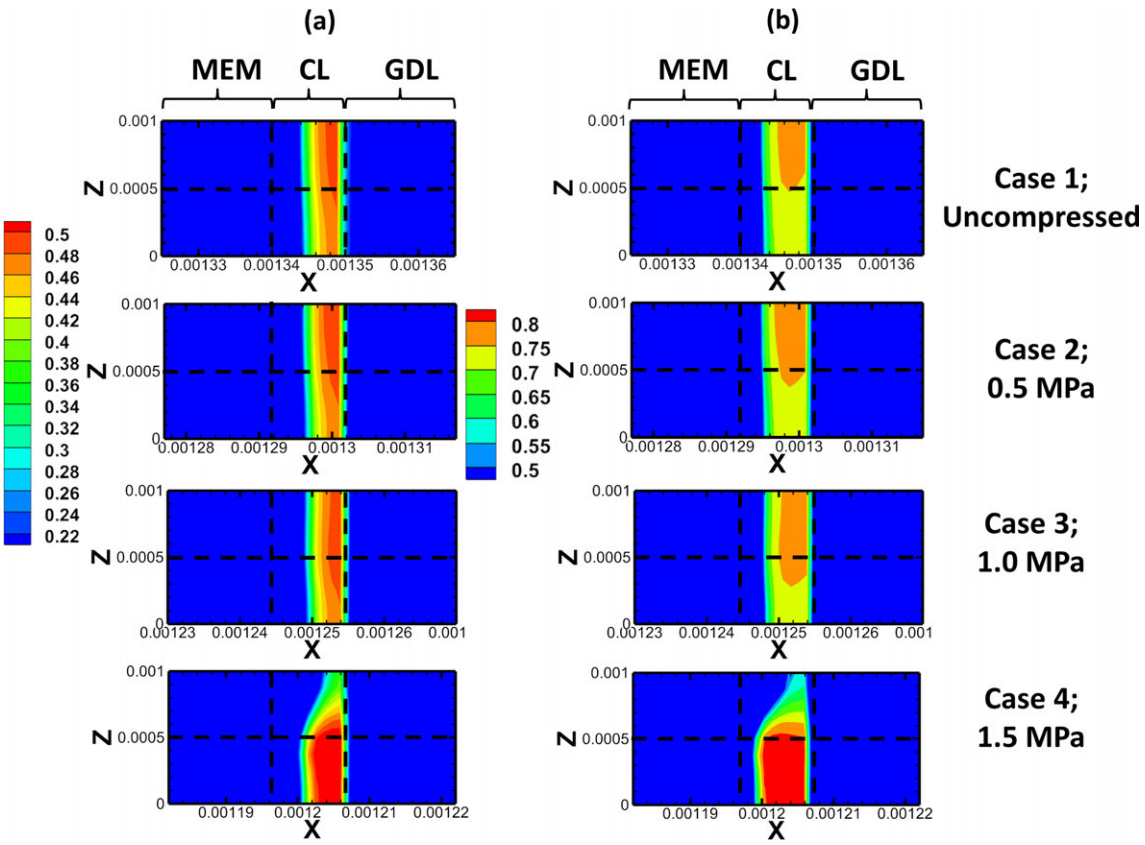

Fig. 5 Ice fraction contours in the cathode CL for cases 1–4 in the mid-*y* *x*–*z* plane at time instants of (a) *t* = 50 s, (b) *t* =76 s under an operating current density of 1,000 A m^{-2}.

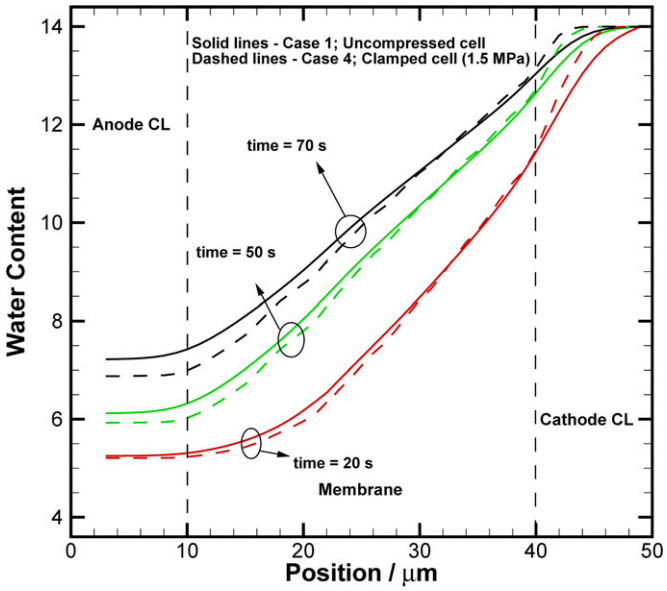

Fig. 6 A comparison of water content profiles between case 1 and case 4 in the MEA at the middle of the fuel cell length along *x*-direction under an operating current density of 1,000 A m^{-2}.

under-land region, the membrane is more humidified and thus has smaller protonic charge transfer resistance, and in this region the electronic charge transport has also shorter transport distance. This situation will not change unless the mass transport is significantly affected by the applied clamping pressure, e.g., for case 4, or a large amount of ice has already formed in the under-land region after long time cold start operation. In addition, it is obvious that the degree of current density uniformity decreases as we increase the applied clamping pressure and it is more critical under the higher operating current load where the oxygen transport resistance is very high. As a result, we conclude that applying an optimum clamping pressure value may result in a more uniform distribution of current density and thereby a better cold start performance.

Generally, the GDL compression improves the electronic conductivity of the GDL because it increases the interfacial contact between neighboring components, hence decreasing the contact resistance between the GDL and bipolar plate, e.g., the contact resistance was 10 mΩ m^2 in case 1 but when the assembly pressure was applied in case 4, the contact resistance was dropped very sharply to 3.79 mΩ m^2. This enhanced electronic conductivity is expected to improve the cell performance. However, the reduced GDL properties such as thickness, porosity and permeability due to GDL compression cause the transport limitation through the GDL. We can observe clearly from Figure 8 that the cold start performance is decreased, and consequently the case with higher clamping pressure exhibits lower cold start performance. In addition, Figure 8 shows that the cold start performance is slightly

ORIGINAL RESEARCH PAPER

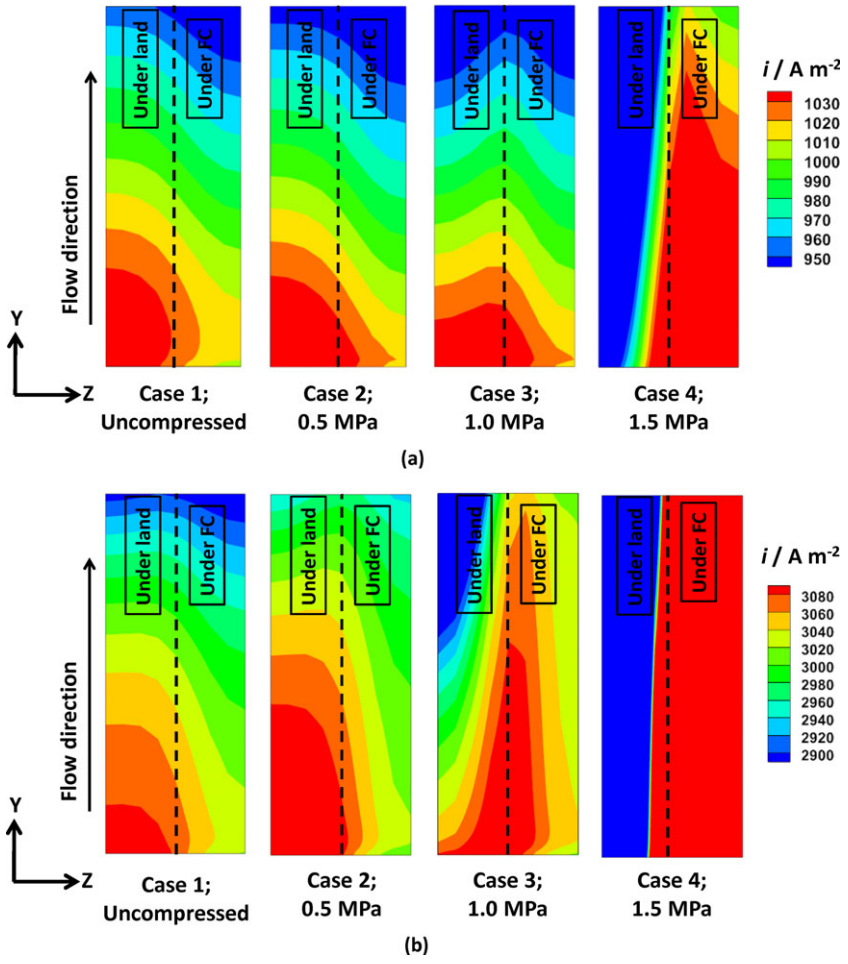

Fig. 7 Current density distribution in the *y*–*z* plane at the center of the membrane under operating current load of (a) 1,000 A m^{-2}, (b) 3,000 A m^{-2} at $t = 30$ s.

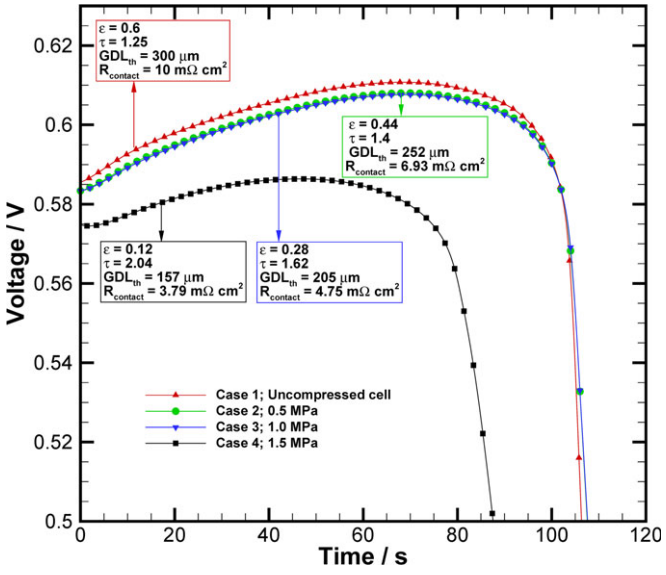

Fig. 8 Cell voltage evaluation curves for different clamping pressures under an operating current density of 1,000 A m^{-2}.

decreased under clamping pressures in a range of 0.5–1.0 MPa. Conversely, applying a clamping pressure of 1.5 MPa has shown a severe degradation on the voltage curve of cold start process.

This implies that the decreased porosity of GDL due to applied clamping pressure is one of the key factors that influence the PEFC cold start performance. Although the generated heat in the cell under different clamping pressures are expected to have a more evident effect, but it shows a small increase in the clamped cases due to the applied quasi-isothermal boundary conditions, and it will be further discussed on a non-isothermal study in future work. More importantly, it is found that under cold start operating conditions the clamping pressure lowers the overall performance and decreases the uniformity in the current density distribution. In addition, the numerical simulation results show much higher cold start performance with the uncompressed case, which overestimates the cell performance, because that does not exist in actual fuel cell performance [39]. Hence, clamping pressure effects on GDL should be considered in cold start fuel cell research.

It is worth mentioning that the trend of cell performance degradation due to clamping pressure was also observed under normal PEFC operating conditions. And the non-deformed case (case 1) was found to have the best cell performance compared to the clamped cases [26, 40, 41]. The clamping pressure was reported to have a direct influence in the reactants transport that caused by the reduced porosity and thickness of GDL. As a consequence, the uniformity of the current density distribution in the membrane was decreased [42, 43].

4 Conclusions

To understand the cold start behavior of PEFC under various clamping pressures, a three-dimensional cold start model is upgraded and further developed, and eight cases are simulated.

The simulation results show that the uncompressed case shows more even distribution of oxygen due to the constant GDL properties under land and channel. It is found that applying a higher clamping pressure increases the degree of non-uniformity in the ice formation contours and current density profiles. Correspondingly, applying a higher clamping pressure results in slightly larger amount of ice in the cathode catalyst layer and the ice tends to accumulate more under the channel region than under the land region owing to the higher current density distribution under the channel, which caused

by the sever oxygen transport limitation under the land region. Furthermore, the existence of higher current density under the channel is found to increase the dragged water by EOD, which exacerbates the dehydration of the membrane in the anode side and results in lower cold start performance. We conclude that applying an optimum clamping pressure value may result in a more uniform distribution of current density and thereby a better cold start performance.

It is interesting to note that the mass transport limitation under clamping pressure plays a dominating role by decreasing the overall performance of cold start process. Although the influence of clamping pressure was neglected in previous published cold start studies, this work reveals that the clamping pressure has a considerable influence in cold start behavior. Additional efforts are underway to consider an inhomogeneous deformation of GDL in order to capture its effect on cold start performance.

Acknowledgments

Financial support received from the China National Key R&D Project (2018YFB0905303, 2018YFB0905300), the Shanghai Automotive Industry Sci-Tech Development Foundation (No. 1706), and the Guangdong Science and Technology Department (2017B010120003, 2016A030313172, 2015A030308019) is gratefully acknowledged.

List of Symbols

A	Area; electrode area / m^2
C	Species concentration / mol m^{-3}
D	Diffusivity / m^2 s^{-1}
E	Elasticity modulus / MPa
EW	Equivalent weight of dry membrane / kg mol^{-1}
F	Faraday constant / C mol^{-1}
i	Current density / A m^{-2}
j	Transfer current density / A m^{-3}
K	Permeability / m^2
n_d	Electroosmotic drag coefficient
p	Pressure / Pa
$\dot{q}$	Water desublimation rate / mol m^{-3} s^{-1}
R	Universal gas constant / J mol^{-1} K^{-1}
s	Ice fraction
S	Source term
t	Time / s
T	Temperature / K
u	Superficial fluid velocity / m s^{-1}

Greek Symbols

ε	Porosity
λ	Water content in membrane
Φ	Phase potential / V
μ	Viscosity / Pa s
ξ	Stoichiometric flow ratio
ρ	Density / kg m^{-3}
η	Overpotential / V
κ	Proton conductivity / S m^{-1}

Superscripts/ Subscripts

e	Electrolyte
eff	Effective
gs	Vapor-solid phase transition
i	Species
mem	Membrane
0	Initial
ref	Reference
s	Solid phase

References

[1] T. Zhang, P. Wang, H. Chen, P. Pei, *Applied Energy* **2018**, *223*, 249.
[2] A. Baroutaji, T. Wilberforce, M. Ramadan, A. Ghani, *Renew. Sustain. Energy Rev.* **2019**, *106*, 31.
[3] Y. Luo, K. Jiao, *Prog. Energy Combust. Sci.* **2018**, *64*, 29.
[4] S. Ge, C. Y. Wang, *Electrochim. Acta.* **2007**, *52*, 4825.
[5] E. Cho, J.-J. Ko, H. Y. Ha, S.-A. Hong, K.-Y. Lee, T.-W. Lim, I.-H. Oh, *J. Electrochem. Soc.* **2003**, *150*, A1667.
[6] R. C. McDonald, C. K. Mittelsteadt, E. L. Thompson, *Fuel Cells* **2004**, *4*, 208.
[7] A. Nandy, F. Jiang, S. Ge, C.-Y. Wang, K. S. Chen, *J. Electrochem. Soc.* **2010**, *157*, B726.
[8] K. Jiao, X. Li, *Int. J. Hydrogen Energy* **2009**, *34*, 8171.
[9] F. Jiang, W. Fang, C.-Y. Wang, *Electrochim. Acta* **2007**, *53*, 610.
[10] K. Tajiri, Y. Tabuchi, F. Kagami, S. Takahashi, K. Yoshizawa, C. Y. Wang, *J. Power Sources* **2007**, *165*, 279.
[11] K. Jiao, X. Li, *Int. J. Hydrogen Energy* **2010**, *35*, 5077.
[12] Q. Yan, H. Toghiani, Y. W. Lee, K. Liang, H. Causey, *J. Power Sources* **2006**, *160*, 1242.
[13] X. G. Yang, Y. Tabuchi, F. Kagami, C.-Y. Wang, *J. Electrochem. Soc.* **2008**, *155*, B752.
[14] Y. Tabe, K. Yamada, R. Ichikawa, Y. Aoyama, K. Suzuki, T. Chikahisa, *J. Electrochem. Soc.* **2016**, *163*, F1139.
[15] L. Mao, C.-Y. Wang, Y. Tabuchi, *J. Electrochem. Soc.* **2007**, *154*, B341.
[16] J. Hou, H. Yu, S. Zhang, S. Sun, H. Wang, B. Yi, P. Ming, *J. Power Sources* **2006**, *162*, 513.
[17] F. Jiang, C.-Y. Wang, *J. Electrochem. Soc.* **2008**, *155*, B743.
[18] F. Jiang, C.-Y. Wang, K. S. Chen, *J. Electrochem. Soc.* **2010**, *157*, B342.
[19] Y. Zhou, K. Jiao, Q. Du, Y. Yin, X. Li, *Int. J. Hydrogen Energy* **2013**, *38*, 12891.
[20] A. M. Dafalla, F. Jiang, *Int. J. Hydrogen Energy* **2018**, *43*, 2327.
[21] P. Zhou, C. W. Wu, G. J. Ma, *J. Power Sources* **2006**, *159*, 1115.
[22] P. Zhou, C. W. Wu, *J. Power Sources* **2007**, *170*, 93.

[23] P. Zhou, C. W. Wu, G. J. Ma, *J. Power Sources* **2007**, *163*, 874.
[24] B. Liu, M. Y. Wei, W. Zhang, C. W. Wu, *J. Power Sources* **2016**, *303*, 118.
[25] D. H. Ahmed, H. J. Sung, J. Bae, *Int. J. Hydrogen Energy* **2008**, *33*, 3786.
[26] I. Taymaz, M. Benli, *Energy* **2010**, *35*, 2134.
[27] W. R. Chang, J. J. Hwang, F. B. Weng, S. H. Chan, *J. Power Sources* **2007**, *166*, 149.
[28] P. H. Chi, S. H. Chan, F. B. Weng, A. Su, P. C. Sui, N. Djilali, *Int. J. Hydrogen Energy* **2010**, *35*, 2936.
[29] Z. Yang, Q. Du, S. Huo, K. Jiao, *Int. J. Hydrogen Energy* **2017**, *42*, 25372.
[30] J. Wang, J. Yuan, B. Sundén, *Int. J. Energy Res.* **2017**, *41*, 985.
[31] P. Taylor, T. Ozgumus, M. Mobedi, U. Ozkol, *Eng. Appl. Comp. Fluid* **2014**, *8*, 308.
[32] R. Bouchet, M. Barrande, R. Bouchet, R. Denoyel, *Anal. Chem.* **2007**, *79*, 9115.
[33] L. Mao, *Ph.D. Thesis*, The Pensssylvania State University, Pensssylvania, USA **2006**.
[34] K. Jiao, X. Li, *Int. J. Hydrogen Energy* **2010**, *35*, 5077.
[35] J. Ko, H. Ju, *Int. J. Hydrogen Energy* **2013**, *39*, 2854.
[36] S. Ge, C. Y. Wang, *Electrochim. Solid-state Lett.* **2007**, *9*, A499.
[37] K. Tajiri, Y. Tabuchi, C. Y. Wang, *J. Electrochem. Soc.* **2007**, *154*, B147.
[38] L. Mao, C. Wang, *J. Electrochem. Soc.* **2007**, *154*, B139.
[39] P. Chippar, K. Oh, D. Kim, T. Hong, W. Kim, H. Ju, *Int. J. Hydrogen Energy* **2012**, *38*, 7715.
[40] S. Toghyani, F. Moradi Nafchi, E. Afshari, K. Hasanpour, E. Baniasadi, S. A. Atyabi, *Int. J. Hydrogen Energy* **2018**, *43*, 4534.
[41] M. Movahedi, A. Ramiar, A. A. Ranjber, *Energy* **2018**, *142*, 617.
[42] Y. Zhou, G. Lin, A. J. Shih, S. J. Hu, *J. Fuel Cell Sci. Technol.* **2009**, *6*, 041005.
[43] J. Wang, J. Yuan, J.-S. Yu, B. Sundén, *Int. J. Energy Res.* **2017**, *41*, 2121.

